

Motion of halo compact objects in the gravitational potential of a low-mass model of the Galaxy

Szymon Sikora

Astronomical Observatory, Jagellonian University, Orla 171, PL-30244 Kraków, Poland

Łukasz Bratek

Institute of Nuclear Physics, Polish Academy of Sciences, Radzikowskiego 152, PL-31342 Kraków, Poland

Lukasz.Bratak@ifj.edu.pl

Joanna Jałocha

Institute of Nuclear Physics, Polish Academy of Sciences, Radzikowskiego 152, PL-31342 Kraków, Poland

Marek Kutschera

Institute of Physics, Jagellonian University, Reymonta 4, PL-30059 Kraków, Poland

ABSTRACT

Recently, we determined a lower bound for the Milky Way mass in a point mass approximation. This result was obtained for most general spherically symmetric phase-space distribution functions consistent with a measured radial velocity dispersion. As a stability test of these predictions against a perturbation of the point mass potential, in this paper we make use of a representative of these functions to set the initial conditions for a simulation in a more realistic potential of similar mass and accounting for other observations. The predicted radial velocity dispersion profile evolves to forms still consistent with the measured profile, proving structural stability of the point mass approximation and the reliability of the resulting mass estimate of $\sim 2.1 \times 10^{11} M_{\odot}$ within 150 kpc. We also find an interesting coincidence with the recent estimates based on the kinematics of the extended Orphan Stream. As a byproduct, we obtain the equations of motion in axial symmetry from a nonstandard Hamiltonian, and derive a formula in the spherical symmetry relating the radial velocity dispersion profile to a directly measured kinematical observable.

Subject headings: techniques: radial velocities - Galaxy: halo - Galaxy: disk - Galaxy: kinematics and dynamics - Galaxy: fundamental parameters - methods: numerical

1. Introduction

Compact objects orbiting the Milky Way can be used to infer the gravitational field at large Galactocentric radii. Jeans modeling links the field with the available kinematical data, under the important assumption that these objects can be described by a collision-less system of test bodies in a steady-state equilibrium (Jeans 1915). Primary in this approach is a *Phase-space Distribution Function (PDF)*, while the physical observables (e.g., the number density, the velocity dispersion ellipsoid, etc.) are *secondary quantities* being PDF-dependent functionals on the phase space.

Galaxy mass can be estimated based on the *Radial Velocity Dispersion (RVD)* data. In the literature, one can find mass values of $4.2^{+0.4}_{-0.4} \times 10^{11} M_{\odot}$ (Deason et al. 2012a), $4.9^{+1.1}_{-1.1} \times 10^{11} M_{\odot}$ (Kochanek 1996), $5.4^{+0.2}_{-3.6} \times 10^{11} M_{\odot}$ (Wilkinson & Evans 1999) and $5.4^{+0.1}_{-0.4} \times 10^{11} M_{\odot}$ (Sakamoto et al. 2003), all within 50 kpc, $4.0^{+0.7}_{-0.7} \times 10^{11} M_{\odot}$ within 60 kpc (Xue et al. 2008), or $(5.8 - 6.0) \times 10^{11} M_{\odot}$ enclosed within 100 kpc (Klypin et al. 2002), whereas, depending on the

model assumptions, the virial mass is $(8 - 10 - 12) \times 10^{11} M_{\odot}$ (Battaglia et al. 2005; Xue et al. 2008; Kafle et al. 2014) or even $(18 - 25) \times 10^{11}$ (Sakamoto et al. 2003). It is noteworthy that the kinematics of extended Orphan Stream indicates the mass of $\sim 2.7 \times 10^{11} M_{\odot}$ within 60 kpc (with disk+bulge mass of $1.3 \times 10^{11} M_{\odot}$) (Newberg et al. 2010; Sesar et al. 2013), significantly less than suggested by the above estimates within 50 kpc. This, points to some model-dependent effects.

In this context it is natural to ask what is the lower bound for the Galaxy mass indicated by the kinematics of the outermost tracers, paying more attention on the phase space model rather than the particular mass model.

With the simplest working hypothesis of absence of the extended halo, the Galactic gravitational field at large distances, to a fair degree of approximation, would be that of a point mass. In this approximation, decisive for the field asymptotics of any compact mass distribution is a single total mass parameter. Bahcall & Tremaine (1981) proposed in this approximation for the neighboring galaxies a mass esti-

mator $\frac{C}{G} \langle v_z^2 R \rangle$, with the averaging performed over distant tracers at various projected radii R , where C is a constant. More recently, Watkins et al. (2010) considered a spherical symmetric counterpart of this estimator, $\frac{C}{G} \langle v_r^2 r^\gamma \rangle$, with an arbitrary power of the radial distance r .

Mass estimators based on Jeans theory, irrespectively of the adopted mass model, are related to a *PDF* restricted in a particular way by some indirect constraints appearing because of the assumptions made about the secondary quantities. The restrictions usually concern the flattening of the velocity dispersion ellipsoid β . This quantity is poorly known for peripheral tracers. Introducing a variable β leads to difficulties in solving the Jeans problem. To overcome this, β is often assumed to be a position independent parameter. On the other hand, this is too much constraining an assumption, since any limitation on β indirectly imposes restrictions on the function space admissible for *PDF*'s. We conjectured (Bratek et al. 2014) that the lower bound for the total mass may increase in response to these constraints, while there is no definite upper bound. In consequence of this the mass is likely to be overestimated.

Recently, there is a growing interest in methods of determining the general assumption-free *PDF*'s from the kinematical data. Magorrian (2014) proposed a framework in which the gravitational potential is inferred from a discrete realization of the unknown distribution function by using snapshots of stellar kinematics. Our previous article (Bratek et al. 2014) is placed within this field of interest. Therein, we proposed a method of determining *PDF*'s from a given spherically symmetric *RVD* profile, without imposing any constraints on the secondary quantities. Even in the simplest case of a point mass approximation, our method allowed to faithfully reconstruct the shape of the *RVD* profile, including its low-size and variable features. By considering various *PDF*'s giving rise to *RVD*'s overlapping with that observed at larger radii, we showed that there is no upper bound for the total mass, while there is a sharp lower bound, slightly below $2.0 \times 10^{11} M_\odot$. For lower masses, no *PDF* could be found to account for the measured *RVD* within the acceptable limits.

1.1. The aim of the present work

The lower bound referred to above may also suggest a Galaxy mass lower than given in the literature. A natural question arises whether it is physically reasonable and could appear in other models? This cannot be excluded. A mass $(2.4 - 2.6) \times 10^{11}$ would be consistent with past results – in a three-component mass model (Merrifield 1992), with the best estimate in the point mass field (Little & Tremaine 1987) – and most remarkably, with the recent value inferred from the kinematics of the Orphan stream (Newberg et al. 2010; Sesar et al. 2013).

Interestingly, the lower bound coincides with the sum of the dynamical mass $\approx 1.5 \times 10^{11} M_\odot$ inferred from the rotation curve in disk model (Jalocha et al. 2014; Sikora et al. 2012) and the mass $(1.2 - 6.1) \times 10^{10} M_\odot$ of the hot gaseous halo surrounding Milky Way (Gupta et al. 2012). The gravitational potential of these components can be interpreted as a perturbation of a point mass potential. But for com-

plicated potentials, the distribution integral on the phase space cannot be explicitly constructed, because the first integrals characterizing admissible orbits are not known in an explicit form. To overcome this difficulty, a numerical simulation can be performed.

In this paper we present an example of such a simulation in which the test bodies represent the compact objects orbiting the Galaxy. The initial conditions for the simulation in the perturbed field should be chosen close to a known stationary solution of Jeans problem in the non-perturbed field. For this purpose we make use of a *PDF* to be found similarly as in (Bratek et al. 2014). But it is not obvious if this initial *PDF* and the resulting *RVD* profile would be stable against such a perturbation. Running a simulation with an initial *PDF* consistent with the observed high *RVD* could lead to an *RVD* profile with quickly and steadily decreasing value. If this happened, this would mean that the initial approximation was far from a stationary solution in the new potential. The main goal of the present paper is to investigate this stability issue and thus also the reliability of the point mass approximation, that is, we test whether predictions for the *RVD* and the mass in the new potential are comparable to those made in the point mass approximation, that is, we test *structural stability* of these predictions.

The structure of this paper is the following. In Sect. 2 we recall the main ideas behind the *Keplerian ensemble method* of obtaining a *PDF*. In Sect. 3, we use a representative of possible *PDF*'s to set the initial conditions for our n-body simulation in the modified potential, next we test stability of the resulting *RVD* profile. Then conclusions follow.

2. First approximation of *PDF* from the Keplerian Ensemble Method

Mathematical preliminaries.¹ An elliptic orbit of a test body bound in the field of a point mass M is fully characterized by 5 integrals of motion: the Euler angles (Φ, Θ, Ψ) determining the orbit orientation, the eccentricity e describing the orbit flattening, and the dimensionless energy parameter $\epsilon = -\frac{RE}{GM}$ describing the size of the large semi-axis (R is an arbitrary unit of length while E is the energy per unit mass). A spherically symmetric collection of confocal ellipses we call *Keplerian ensemble*. From Jeans (1915) theorem, for this ensemble in a steady state equilibrium it suffices to consider *PDF*'s being functions of e and ϵ only. Accordingly, instead of $r, \theta, \phi, v_r, v_\theta, v_\phi$ we use phase coordinates $u, \theta, \phi, e, \epsilon, \psi$ defined by:

$$\begin{aligned} r &= Ru, & v_r^2 &= \frac{GM}{R} \left(\frac{2}{u} - \frac{1-e^2}{2\epsilon u^2} - 2\epsilon \right), \\ (v_\theta, v_\phi) &= \frac{1}{u} \sqrt{\frac{GM}{R}} \left(\frac{1-e^2}{2\epsilon} \right)^{1/2} (\sin \psi, \cos \psi). \end{aligned} \quad (2-1)$$

For physical reasons we assume all orbits to be confined entirely within a region $u \in (u_a, u_b)$ bounded by two spheres of radii u_a and u_b . This way all orbits with too low pericentra (i.e., violating the point mass approximation) or

¹This paragraph summarizes the mathematical basis of our method discussed in a more detail in (Bratek et al. 2014).

with too high apocentra (e.g. beyond Local Group members) are excluded. Consequently, the space of parameters (e, ϵ) gets restricted to a domain S : $\frac{1+\epsilon}{2u_b} < \epsilon < \frac{1-\epsilon}{2u_a}$ and $0 \leq e < \frac{u_b - u_a}{u_b + u_a} < 1$. On integrating out the angles θ, ϕ, ψ , the principal integral $\int f(\vec{r}, \vec{v}) d^3\vec{r} d^3\vec{v}$ reduces (to within an unimportant constant factor) to

$$\int_{u_a}^{u_b} \nu_u[f] du, \quad \nu_u[f] \equiv \int_{S(u)} \frac{e de d\epsilon f(e, \epsilon)}{\sqrt{\epsilon \left(\epsilon - \frac{1-\epsilon}{2u}\right) \left(\frac{1+\epsilon}{2u} - \epsilon\right)}}. \quad (2-2)$$

The integration domain $S(u) \subset S$ is a u -dependent quadrilateral region $\epsilon \in \left(\text{Max}\left(\frac{1-\epsilon}{2u}, \frac{1+\epsilon}{2u_b}\right), \text{Min}\left(\frac{1+\epsilon}{2u}, \frac{1-\epsilon}{2u_a}\right)\right)$, $e \in \left(0, \frac{u_b - u_a}{u_a + u_b}\right)$, each point of which corresponds to a spherically symmetric pencil of confocal elliptical orbits intersecting a sphere of a certain radius u . The functional $\nu_u[f]$ has the interpretation of the probability density for the variable r/R to fall within the spherical shell $u < r/R < u + du$.

Given a *PDF* $f(e, \epsilon)$, the expectation value $\langle g \rangle_r$ for an observable $g = g(e, \epsilon, u)$ inside that shell equals

$$\langle g \rangle_r = \frac{\nu_u[fg]}{\nu_u[f]}. \quad (2-3)$$

In particular, given M and $f(e, \epsilon, u)$, the model *RVD* profile $\langle r v_r^2 \rangle / G$ is obtained with $g(e, \epsilon, u) \equiv \frac{r v_r^2}{GM} = 2 - \frac{1-\epsilon^2}{2\epsilon u} - 2\epsilon u$ substituted for g in Eq. 2-3.²

But we are concerned with the inverse problem: given an *RVD* profile matching the observations, we want to derive a distribution function f the *RVD* profile would follow from. This problem can be solved as follows. First, we consider an auxiliary function $h(e, \epsilon)$ such that $f = h^2$ (then $f \geq 0$, as required for a probability density) and make a series expansion in polynomials \mathcal{Q}_k orthogonal on S :

$$h(e, \epsilon) \approx \sum_{k=1}^{D_d} h_k \mathcal{Q}_k(e, \epsilon). \quad (2-4)$$

The \mathcal{Q}_k 's are constructed with the help of a Gram-Schmidt orthogonalization method on S . Next, given a mass parameter M , we find an optimum sequence of expansion coefficients h_k by minimizing a discrepancy measure between $a)$ the *RVD* profile from measurements, $\bar{p}_r \equiv \overline{r v_r^2} / G$, where the averaging is taken over all halo compact objects within a spherical shell of some width and a given radius r , and $b)$ the model $\langle g \rangle_r$ profile calculated from Eq. 2-3 with the help of the function h corresponding to the optimum h_k 's. With these h_k 's, the discrepancy measure can be reduced further by replacing M with a better fit value, e.g., $M \rightarrow M_{bf} = \frac{\sum_r \langle g \rangle_r \bar{p}_r}{\sum_r \langle g \rangle_r^2}$ if the $\sum_r (M \langle g \rangle_r - \bar{p}_r)^2$ norm is used.

This way, a *PDF* $f(e, \epsilon)$ consistent with the *RVD* measurements can be reconstructed, provided M is large enough. For M above a limiting value M_{cut} there is always a *PDF* for which the *RVD* profile is perfectly accounted for, while below this limit no satisfactory fit can be found. For $M > M_{\text{cut}}$, increasing the number D_d of the basis polynomials \mathcal{Q}_k , efficiently decreases the fit residuals, but for D_d high enough

the residuals appear to tend to some small nonzero limit. For $M < M_{\text{cut}}$ the fit residuals remain very large, regardless of D_d , and rapidly increase with decreasing M . This shows that M_{cut} is the lower bound for the mass in the point mass approximation.

2.1. RVD profile from measurements

Without transverse velocity components, the radial motions of kinematic tracers cannot be unambiguously transformed from the *LSR* frame to the Galactocentric frame. However, for a spherically symmetric distribution of tracers one can try to assume a $\beta(r)$ profile or find a self-consistent one by iterations. The particular model of $\beta(r)$ affects the *RVD* significantly only inside a spherical region of several r_\odot in diameter. But we must bear in mind a twofold influence of the particular model of β on the total mass determination: both $\beta(r)$ itself and the so obtained β -dependent *RVD* profile enter the spherical Jeans equations.

2.1.1. A formula relating the *LSR* radial motion measurements to the Galacto-centric *RVD*

Here, we consider a spherically symmetric ensemble of test bodies described by some *PDF* and the resulting $\beta(r)$, then also $\langle v_\phi^2(r) \rangle = \langle v_\theta^2(r) \rangle$ (averaging over spherical shells). For a test body with a velocity vector \vec{v} in the Galactocentric coordinate frame, the radial and tangential components of \vec{v} are $v_r = \vec{v} \circ \vec{e}_r$, $v_\theta = \vec{v} \circ \vec{e}_\theta$, $v_\phi = \vec{v} \circ \vec{e}_\phi$, with $\vec{e}_r = \frac{\vec{r}}{|\vec{r}|}$, $\vec{e}_\theta, \vec{e}_\phi$ forming an orthonormal basis tangent to the lines of constant spherical coordinates r, θ, ϕ . Although \vec{v} can be determined for closer objects, only its projection $\tilde{v}_r = \vec{v} \circ \vec{e}_r$ onto the line of sight determined by the unit vector $\vec{e}_r = \frac{\vec{r} - \vec{r}_\odot}{|\vec{r} - \vec{r}_\odot|}$ can be measured for all objects. This is the only kinematical information available at large distances, suitable for constraining the total Galactic mass. It is connected with direct measurements of the *LSR* relative velocity v_ρ along the direction \vec{e}_ρ through the relation $\tilde{v}_r = v_\rho + \vec{v}_\odot \circ \vec{e}_\rho$.

Assuming a $\beta(r)$, we can relate $\langle \tilde{v}_r^2(r) \rangle$ to $\langle v_r^2(r) \rangle$ through the following identity true both for $r < r_\odot$ and $r > r_\odot$:

$$\langle \tilde{v}_r^2(r) \rangle = \langle v_r^2(r) \rangle \left(1 - \frac{\beta(r)}{4} H(r/r_\odot) \right) \quad (2-5)$$

$$H(x) = 1 + x^{-2} - \frac{(x^2 - 1)^2}{2x^3} \ln \left| \frac{x+1}{x-1} \right|.$$

For the isotropic dispersion, $\beta(r) = 0$, we can formally make the (incorrect) identification $\tilde{v}_r = v_r$ globally, without making any error in equating the resulting dispersions $\langle \tilde{v}_r^2 \rangle = \langle v_r^2 \rangle$. For large r , $H \sim 1 - \beta(r) \frac{2r_\odot^2}{3r^2} \rightarrow 1$ if β is asymptotically bound (which may not hold for nearly circular orbits). Battaglia et al. (2005) derived a similarly looking result only for $r > r_\odot$, concluding – counter to Eq. 2-5 and the geometric intuition – that $\langle v_r^2(r) \rangle$ and $\langle \tilde{v}_r^2(r) \rangle$ coincided for purely radial anisotropic ellipsoid ($\beta = 1$), not for purely isotropic ones ($\beta = 0$). To dispel doubts as to which conclusion is correct, we present our derivation of Eq. 2-5 in Appendix A.

While determining a *PDF* $f = f(\vec{r}, \vec{v})$ from the $\langle \tilde{v}_r^2(r) \rangle$ observable, a self-consistent $\beta(r)$ may be looked for by iterations. The first recursion step makes the assumption

²In place of (e, ϵ, u) it is more convenient the use of coordinates (α, β, u) , such that $e = \frac{\beta - \alpha}{\beta + \alpha}$, $\epsilon = \frac{1}{u} \frac{\alpha \beta}{\alpha + \beta}$. A motivation behind this mapping and its explicit construction is given in (Bratek et al. 2014).

$\langle v_r^2(r) \rangle = \langle \tilde{v}_r^2(r) \rangle$ as if $\beta(r) = 0$, and a first approximation to f is obtained, from which a $\beta(r)$ prediction for the next iteration step is calculated. Substituted in Eq. 2-5, the $\beta(r)$ gives rise to a new $\langle v_r^2(r) \rangle$. The process is repeated until a stable $\beta(r)$ is reached. However, the distinction between $\langle v_r^2(r) \rangle$ and $\langle \tilde{v}_r^2(r) \rangle$ is practically unimportant, unless the lower radii region is considered. In preparing the RVD profile below, we may neglect this distinction.

2.1.2. Measurements data

In our previous work (Bratek et al. 2014) we determined a RVD profile Fig. 1 which we now assume as the basis for generating the initial conditions for the simulation in Sect. 3.1, and use it as a reference profile for comparison with the simulation results in Sect. 3.4. We obtained this profile with the

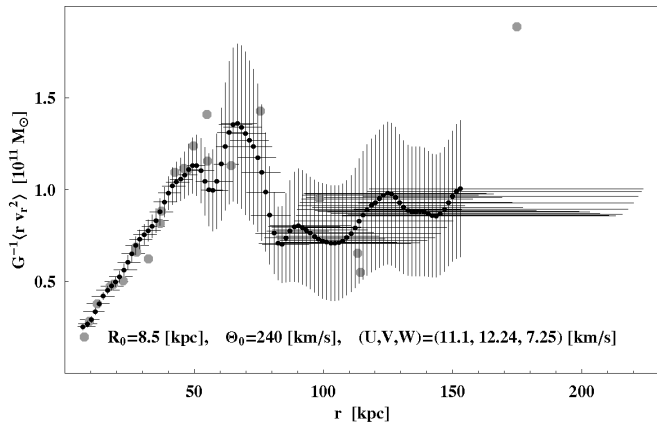


Fig. 1.— RVD profile $G^{-1}(r \langle v_r^2 \rangle)$ for tracers with $\frac{1}{2G} r v_r^2 \lesssim 3.5 \times 10^{11} M_{\odot}$. The horizontal bars represent the effective radial bin size of the moving average. The vertical bars indicate the spread in the profile due to the inclusion/exclusion of random subsets of tracers. A detailed description of how this profile was obtained is given in (Bratek et al. 2014). As reference values, we show $G^{-1} r \langle v_r^2 \rangle$ calculated based on the RVD points in (Xue et al. 2008) and (Deason et al. 2012b) [large gray circles]

use of the following position-velocity data: the halo giant stars (Dohm-Palmer et al. 2001; Starkenburg et al. 2009) from the Spaghetti Project Survey (Morrison et al. 2000); the blue horizontal branch stars (Clewley et al. 2004) from the United Kingdom Schmidt Telescope observations and SDSS; the field horizontal branch and A-type stars (Wilhelm et al. 1999) from the Beers et al. (1992) survey; the globular clusters (Harris 1996) and the dwarf galaxies (Mateo 1998). The data were recalculated to epoch J2000 when necessary. In addition, we included the ultra-faint dwarf galaxies such as Ursa Major I and II, Coma Berenices, Canes Venatici I and II, Hercules (Simon & Geha 2007), Bootes I, Willman 1 (Martin et al. 2007), Bootes II (Koch et al. 2009), Leo V (Belokurov et al. 2008), Segue I (Geha et al. 2009), and Segue II (Belokurov et al. 2009). To eliminate a possible decrease in the RVD at lower radii due to circular orbits in the disk, we excluded tracers in a neighborhood $(R/20)^2 + (Z/4)^2 < 1$ (in units of kpc) of the mid-plane. We also did not take into account: *a*) a distant Leo T located at $r > 400$ kpc, *b*) Leo I, rejected for reasons largely discussed in (Bratek et al. 2014), *c*) a single star for which $r v_r^2 / (2G) > 5.6 \times 10^{11} M_{\odot}$, and *d*)

4 additional objects for which $r v_r^2 / (2G) \gtrsim 3.5 \times 10^{11} M_{\odot}$ (these are: 88-TARG37, Hercules, J234809.03-010737.6 and J124721.34+384157.9). As shown with the help of a simple asymptotic estimator (Bratek et al. 2014), had we not excluded *d*) the total expected mass would have been increased by only a factor of ≈ 1.16 .

3. Simulation of RVD in a background field

We model the Galactic potential as consisting of: a disk-like component (accounting for the Galactic rotation curve) and a hot gaseous halo, $\Psi = \Psi_{\text{disk}} + \Psi_{\text{gas}}$, of total mass $M_{\text{ref}} = 1.8 \times 10^{11} M_{\odot}$. As a starting point for further analyses, we construct an initial PDF by applying the method of Sect. 2 to the RVD profile in Fig. 1, assuming $M = M_{\text{ref}}$, which is close to the lower bound for this RVD. In Fig. 2 we show the resulting PDF on the (e, ϵ) plane.

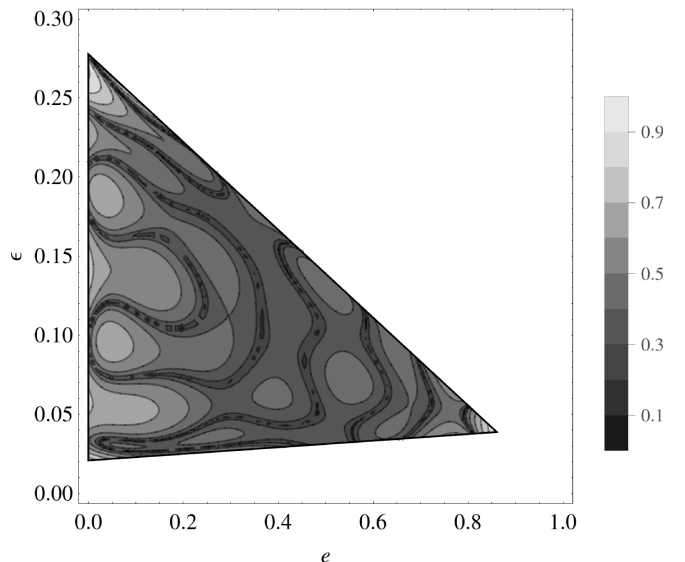


Fig. 2.— A distribution function $f(e, \epsilon)$ consistent with the RVD profile shown in Fig. 1. The function was obtained with the help of the Keplerian ensemble method, assuming $M_{\text{ref}} = 1.8 \times 10^{11} M_{\odot}$, $Ru_a = 18$ kpc and $Ru_b = 240$ kpc. The contour plot shows $(f(e, \epsilon) / f_S)^{1/10}$, with f_S being the maximum value of $f(e, \epsilon)$ on the triangular domain.

3.1. Setting the initial conditions

The first stage toward determining the initial conditions corresponding to the PDF $f(e, \epsilon)$ shown in Fig. 2 involves generating a random set of initial radii $\mathcal{I}_0 = \{u_i\}_{i=1}^N$ in the range $u_a < u_i < u_b$ (N is the number of all test bodies), and with the number density $\nu_u[f]$ from Eq. 2-2. This task of generating random numbers non-uniformly distributed in a range can be solved as follows. Once we find an approximate function interpolating an array of P pairs $\{(u_p, x'_p \equiv \nu_{u_p}[f])\}_{p=1}^P$ ordered w.r.t the first argument, we can compute, by numerical integration, an array consisting of triples

$$\{(x_p = \int_{u_a}^{u_p} \nu_{\tilde{u}}[f] d\tilde{u}, u_p, u'_p = (x'_p)^{-1} = (\nu_{u_p}[f])^{-1})\}_{p=1}^P,$$

and finally, by a suitable procedure interpolating between the knot points u_p , we obtain a smooth function $u(x)$. With a version of a quartic spline interpolation, we can obtain a

smooth $u(x)$ with continuous derivatives up to fourth order (in addition to known tabulated $u(x)$ we know also its derivative $u'(x) \equiv 1/x'(u)$). Provided that $\nu_{u_p}[f]$ has been normalized to unity, $\int_{u_a}^{u_b} \nu_{\tilde{u}}[f] d\tilde{u} = 1$, the smooth $u(x)$ maps random numbers x uniform in the range $(0,1)$ to random numbers u with the required nonuniform distribution $\nu(u)$ in the range (u_a, u_b) . It may be instructive to note that $u(x)$ is the inverse of the cumulative probability function $\chi(u) \equiv \int_{u_a}^u \nu(\tilde{u}) d\tilde{u}$ of the probability density $\nu(u)$: $x = \chi(u)$.³

In the next stage, we need to ensure spherical symmetry of the initial state. We assign to \mathcal{I}_0 a set $\{(\theta_i, \phi_i)\}_{i=1}^N$ of spherical coordinates of directions uniformly distributed on the unit sphere. From the general result in footnote 3 it follows that if $\theta = \arccos(1 - 2x)$ and $\phi = 2\pi y$, then (θ, ϕ) will be uniformly distributed on the unit sphere once both x and y are uniformly distributed on independent unit intervals. This gives us the initial positions $\mathcal{I}_1 = \{(u_i, \theta_i, \phi_i)\}_{i=1}^N$.

Next, to obtain initial velocities, we choose random parameters (e, ϵ, ψ) consistently with the initial PDF, assigning to each $(u_k, \theta_k, \phi_k) \in \mathcal{I}_1$ an elliptic orbit a particular test body would follow in the point mass field. To this end we consider triples of random numbers (e, ϵ, X) uniformly distributed in their respective range: $e \in (0, 1)$, $\epsilon \in (0, 1/(2u_a))$ and $X \in (0, f_S)$, with X being an auxiliary variable and $f_S = \max\{f(e, \epsilon): (e, \epsilon) \in S\}$. For each $u_k \in \mathcal{I}_0$ we carry on generating random triples (e, ϵ, X) until we encounter one (labeled with a subscript k) for which both $X < f(e_k, \epsilon_k)$ and $(e_k, \epsilon_k) \in S(u_k)$. This procedure yields a set of random pairs $\mathcal{I}_2 = \{(e_i, \epsilon_i)\}_{i=1}^N$ with a non-uniform number density distribution $f(e, \epsilon)$ and each confined to a u_i -dependent region $S(u_i)$. To each u_k we also assign its respective random angle ψ_k uniformly distributed in the range $(0, 2\pi]$ and fixing the plane of the corresponding ellipse. In effect, we obtain a set $\mathcal{I}_2 = \{(e_i, \epsilon_i, \psi_i)\}_{i=1}^N$ and form the set $\mathcal{I} = \mathcal{I}_1 \oplus \mathcal{I}_2 = \{(u_i, \theta_i, \phi_i, e_i, \epsilon_i, \psi_i)\}_{i=1}^N$. Finally, by applying the transformation Eq. 2-1 to each element of \mathcal{I} we obtain the required set of initial positions and velocities in spherical coordinates, leading to an initial randomly generated RVD overlapping well with that in Fig. 1 in the region of interest.

3.2. Gravitational potential

The Ψ_{disk} part of Ψ is described by the thin disk model:

$$\Psi_{\text{disk}}(\rho, \zeta) = -4G \int_0^\infty d\tilde{\rho} \frac{\tilde{\rho} K(k) \sigma(\tilde{\rho})}{\sqrt{(\rho + \tilde{\rho})^2 + \zeta^2}}, \quad (3-1)$$

with $\sigma(\rho)$ being the column mass density of a finite-width disk found by recursions from the Galactic rotation curve in (Jałocha et al. 2014). Here, $k = \sqrt{\frac{4\rho\tilde{\rho}}{(\rho+\tilde{\rho})^2 + \zeta^2}}$ and K is the elliptic integral of the first kind defined in (Gradshteyn et al. 2007). Most of the mass is enclosed within

the inner disk $\rho < 20$ kpc: $M_{20} = 1.49 \times 10^{11} M_\odot$, while $M_{30} = 1.51 \times 10^{11} M_\odot$. The outer $\rho > 30$ kpc disk's contribution to Eq. 3-1 is thus negligible and we can limit the integration to $\tilde{\rho} \in (0, 30)$ kpc. To reduce the computation time, we tabulated the integral Eq. 3-1 at mesh points $\{\rho_j, \zeta_k\}$, obtaining a smooth Ψ_{disk} by means of the interpolating series $\tilde{\Psi}_{\text{disk}}(\rho, \zeta) = \sum_{p,q,r} \omega_{pqr} \rho^p \zeta^q (\rho^2 + \zeta^2)^{-r/2}$ with the coefficients ω_{pqr} found by the least squares method, minimizing the discrepancy between Eq. 3-1 and the series evaluated at the mesh points. Within the desired accuracy, we found this approximation procedure to be numerically more efficient than the usual two-dimensional interpolation.

Based on the $\text{O}_{\text{VII}}\text{K}_\alpha$ absorption-line strengths in the spectra of galactic nuclei and galactic sources, Gupta et al. (2012) found large amounts of baryonic mass in the form of hot gas surrounding the Galaxy. Assuming a homogeneous sphere model, they found the electron density n_e of $2.0 \times 10^{-4} / \text{cm}^3$ and the path length L of 72 kpc. Among other parameters, the total mass of the gas depends on the gas metallicity and the oxygen-to-helium abundance. For a reasonable set of parameters they found the total mass to be $1.2 - 6.1 \times 10^{10} M_\odot$. We may assume $M_{\text{gas}} = 3.0 \times 10^{10} M_\odot$ consistently with these values. More recently, by applying the same observational method, Miller & Bregman (2013) found the mass function $M(r)$ of the circumgalactic hot gas using a modified density profile

$$n(r) = n_0 (1 + (r/r_c)^2)^{-3\lambda/2}.$$

We use it as the source of the spherical component $\Psi_{\text{gas}}(r)$, with the parameters $n_0 = 0.46 \text{ cm}^{-3}$, $r_c = 0.35$ kpc and $\lambda = 0.58$ allowable by the best fit to the measurements. Then the integrated mass is $M_{\text{gas}} = 3 \times 10^{10} M_\odot$ at $r = 100$ kpc. For $\lambda \leq 1$, the mass function is divergent and the integration must be cutoff at some radius, which is to some extent arbitrary. The cutoff at 100 kpc falls within the limits 18 kpc and 200 kpc on the minimum and maximum mass of the halo considered in (Miller & Bregman 2013).

3.3. Numerical solution of the equations of motion

We consider a test particle of mass m in cylindrical coordinates (ρ, φ, ζ) , moving in an axi-symmetric gravitational field described by the potential Ψ . In this symmetry, the angular momentum component $J_\varphi = m \rho^2 \dot{\varphi}(t)$ is conserved. On account of φ being a monotone function of the time t for orbits with $J_\varphi \neq 0$, we may regard φ as the independent parameter. In this parametrization, the Hamilton equations reduce to

$$\begin{aligned} \rho'(\varphi) &= \frac{\rho^2}{\mathcal{J}} v_\rho, & v_\rho'(\varphi) &= \frac{\mathcal{J}}{\rho} - \frac{\rho^2}{\mathcal{J}} \partial_\rho \Psi(\rho, \zeta), \\ \zeta'(\varphi) &= \frac{\rho^2}{\mathcal{J}} v_\zeta, & v_\zeta'(\varphi) &= -\frac{\rho^2}{\mathcal{J}} \partial_\zeta \Psi(\rho, \zeta), \end{aligned} \quad (3-2)$$

with $\mathcal{J} = J_\varphi/m$ being the angular momentum per unit mass and v_ρ and v_ζ the velocity variables in the orthonormal basis of the coordinate lines ρ, ζ (see Appendix B for a derivation of this from a nonstandard Hamiltonian). We solve Eq. 3-2 numerically by using a 4-order Runge-Kutta method with adaptive step size. controlled so as to keep below some small threshold value the relative change $|\Delta\mathcal{E}/\mathcal{E}|$ in the energy per

³With any function $\nu(u)$ positive and integrable to unity on an interval (u_a, u_b) a coordinate change $u \rightarrow x = \chi(u)$ can be associated, where $\chi(u) = \int_{u_a}^u \nu(\tilde{u}) d\tilde{u}$ is a growing function of u , $\chi(u_a) = 0$ and $\chi(u_b) = 1$. Let χ^* denote the inverse function of χ : $\chi^*(x) = u$. From the identity $x \equiv \int_0^x 1 d\tilde{x} \equiv \int_{u_a}^u \chi^*(\tilde{u}) d\tilde{u} \equiv \chi(u)$ it simply follows that if x is uniformly distributed on the unit interval $(0, 1)$ then $u = \chi^*(x)$ is distributed with the probability density $\nu(u)$ on the interval (u_a, u_b) .

unit mass $\mathcal{E} = \frac{1}{2} (v_\rho^2 + v_\zeta^2 + \mathcal{J}^2/\rho^2) + \Psi(\rho, \zeta)$. The relative change of energy along each trajectory during our simulation is then always smaller than 10^{-6} : $|\mathcal{E}(t)/\mathcal{E}(0) - 1| < 10^{-6}$ for all t , and this precision suffices for the purposes of this work.

3.4. Results and discussion

Using the numerical procedure of Sect. 3.3, we obtained 3665 trajectories of test bodies starting from the initial conditions of Sect. 3.1 and bound in the potential $\Psi_{\text{disk}} + \Psi_{\text{gas}}$ defined in Sect. 3.2. The initial state agrees with the initial *PDF* (Fig. 2) of a stationary solution of Jeans’s problem in the point mass potential and is consistent with the background Galactic *RVD* (Fig. 1). Using these trajectories, we determined the *RVD* evolution from the initial one and track it through a sequence of snapshots taken at various instants, as shown in Fig. 3 (with a step size of ≈ 1 GY). Each snapshot can be regarded as an independent *RVD* model used to estimate the Galaxy mass by comparing the evolved *RVD* with the background *RVD*. In this approach, the mass we assign to $\Psi_{\text{disk}} + \Psi_{\text{gas}}$ becomes a function of the simulation time, while the extent of that time has no physical meaning.

At this point, it is appropriate to bring to attention some features of the initial *PDF* persisting during the simulation as model effects. Namely, in the lower radii region, the evolved *RVD* values are reduced relative to the background *RVD*. The first reason is that for the initial *PDF* from the point mass approximation, a fraction of objects in the modified potential have too high velocities owing to a more extended mass distribution, and either quickly populate more distant regions or are not bound (in preparing the evolved *RVD* profiles we considered only bound trajectories). Consequently, the higher velocity values do not contribute in this region and the *RVD* values get reduced. The other model effect is due to a cutoff in the *PDF* domain introduced in the Keplerian ensemble method to automatically prevent test bodies from penetrating the interior of a central spherical region where the point mass approximation is violated. As so, there is no limit on the number of almost nearly circular orbits the external neighborhood of this region can accommodate – too much elongated orbits cannot occur there for geometrical reasons, while the admissible elongated orbits enter this region with their pericentric sides only (where radial motions are almost vanishing). In consequence of this, the overall mean *RVD* in this neighborhood gets reduced, below the observed values. Because the initial *PDF* has been identified with the *PDF* of the Keplerian ensemble, a qualitatively similar reduction mechanism in the evolved *RVD* comes about in the modified potential, reflecting in the $\beta(r)$ reduced toward more negative values in the lower radii region (however, more circular motions in this region could be interpreted as consistent with a contribution from a cold disk). With a better initial *PDF* this model effect could be eliminated but it seems of no importance for the accuracy of the total mass determination for which the region of greater radii is more important. A similar cutoff mechanism may increase the number density in the neighborhood of the upper boundary (which we assumed to be of 240 kpc). Namely, the high *RVD* values observed for moderate radii and modeled in the point mass approximation by more elongated

elliptic orbits, are reduced again to zero close to the upper boundary. This reduction in the *RVD* appears naturally – the elongated orbits enter this region with their apocentric sides where radial motions are almost vanishing and where test bodies spent a relatively longer time, and this effect can be amplified by increasing the number density of bodies on more circular orbits. Because the model *RVD* is compared with the measurements at moderate radii, this effect can be again neglected.

Now, let us come back to the main issue. As mentioned earlier, we want to verify the expectation that the evolved *PDF* should be in a sense close to the initial *PDF*, independently of the simulation instant if the point mass approximation well describes the real situation at higher distances. If the *RVD* evolved in the modified potential turned out to be collapsing to much smaller values or change its shape completely, then this would mean that the mass estimate based on the initial *PDF* was wrong and inconsistent with the new evolved *PDF*.

As seen in Fig. 3, although the evolved *RVD* changes with the simulation time – it decreases a little in some region and later it grows again – it generally remains high in the larger radii region. Similarly, the characteristic maxima in the initial *RVD* are not destroyed but oscillate. Besides

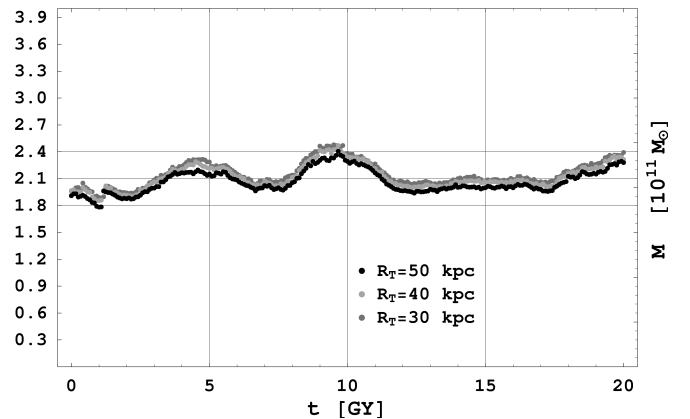


Fig. 4.— Mass estimator μM_{ref} as a function of the simulation time, with factors μ obtained from best fit model *RVD* at various threshold radii R_T .

the evolved *RVD* profile (gray line) corresponding to the mass M_{ref} , in each snapshot there is also shown a corrected *RVD* (thick black-line) which we consider as our model *RVD* profile, obtained by multiplying M_{ref} and the radial variable with suitable factors close to unity, respectively μ and α , so as to make the model *RVD* coincide with the background one as good as possible in the sense of the least squares.⁴ During the simulation run, the length factor α varied in the range (0.85; 1.02) with the mean 0.92 ± 0.03 , while the mass factor μ varied in the range (1.03; 1.37) with the mean 1.18 ± 0.07 (see Fig. 4). This gives the total mass estimate of $(2.12 \pm 0.13) \times 10^{11} M_\odot$, oscillating in the range $(1.85; 2.47) \times 10^{11} M_\odot$.

⁴that is, by minimizing $\delta \equiv M_{\text{ref}}^{-1} [N^{-1} \sum_{i=1}^N (\mu \cdot Y(r_i/\alpha) - Y_o(r_i))^2]^{1/2}$, where $Y(r)$ is the gray line *RVD*, $Y_o(r)$ is the background *RVD*, and the summation is taken over $r_i > R_T$, with a threshold radius $R_T = 40$ kpc delineating the less important lower radii region.

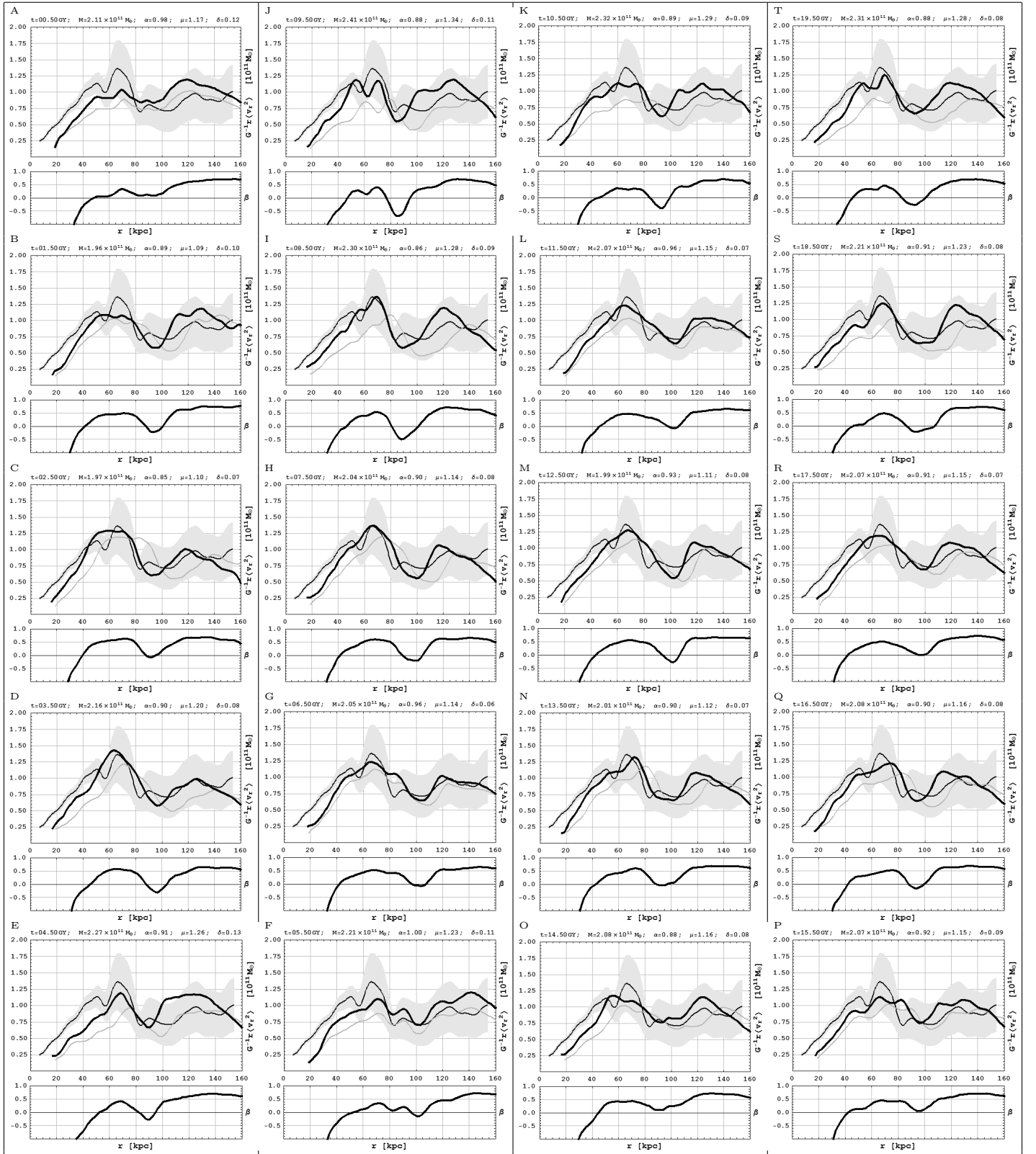


Fig. 3.— A sequence A, B, \dots, S, T of simulated RVD models [thick black lines] shown at distinct simulation instants. The models were obtained from the [gray line] RVD (evolved from the initial PDF in the $\Psi_{\text{disk}} + \Psi_{\text{gas}}$ potential of total mass M_{ref}) by rescaling the horizontal and vertical directions so as to overlap with the background RVD (from measurements) [thin black line] as good as possible. The [light gray region] is the RVD uncertainty defined by the vertical bars in Fig. 1. The bottom figure in each panel shows a $\beta(r)$ profile corresponding to its respective RVD model. The decrease in $\beta(r)$ towards negative values in the lower radii region $r < 40$ kpc is a model effect discussed in the text.

4. Conclusions

The lower bound for the Galaxy mass of $\approx 2.1 \times 10^{11} M_\odot$ obtained within the Keplerian ensemble framework suffices to retain, during a numerical simulation run in a modified potential, the qualitative features of the evolved *RVD* profile and its values, consistently with the *RVD* from halo measurements within 150 kpc. In this sense the evolved *RVD* is stable. These results also substantiate structural stability of the point mass approximation, showing that the lower range for Galaxy mass estimates assuming more general unconstrained *PDF*'s in this approximation is reliable. A possible correction factor 1.16 to account for the 4 halo objects rejected in Sect. 2.1.2, would give a value of $(2.5 \pm 0.2) \times 10^{11}$, consistently with earlier estimates of $2.4 \times 10^{11} M_\odot$ (Merrifield 1992; Little & Tremaine 1987) or with the value of $(2.6-2.7) \times 10^{11} M_\odot$ recently inferred from the kinematics of the Orphan stream (Newberg et al. 2010; Sesar et al. 2013) within ~ 60 kpc.

The crucial role in our analysis is played by the general unconstrained phase space. We stress that the phase space model is not less important than the mass model, and focusing more attention on generic phase spaces might help to reduce the missing mass problem.

We are aware of that the model potential considered here neglects the nonbaryonic dark matter (NDM) halo thought to extend to very large distances. However, this is the most hypothetical and less constrained Galactic component. As we mentioned in Sect. 1, the Galaxy mass estimates in the literature differ between each other by a factor larger than two. We presented here the extreme example of a model without NDM halo, and have shown the model to be stable in a sense that it accounts for the measured *RVD* at each simulation instant. This shows that our model can be thought of as a collision-less system close to a steady-state. The possibility of accounting for the *RVD* observations without NDM halo shows that either the halo is not necessary for understanding motions of the kinematical tracers, or that other observational features (e.g. the measurements of the $\beta(r)$ function) are needed in order to define constraints on the phase space which would allow to disambiguate between various halo mass profiles.

APPENDIX

A. Derivation of a relation between the observable $\langle \tilde{v}_r^2 \rangle$ and the radial dispersion $\langle v_r^2 \rangle$

Let \vec{v} be the Galacto-centric velocity vector. Expressed in terms of its radial V_r and transversal components V_θ, V_ϕ it reads $\vec{v} = [V_r \sin \theta \cos \phi + V_\theta \cos \theta \cos \phi - V_\phi \sin \phi, (V_r \sin \theta + V_\theta \cos \theta) \sin \phi + V_\phi \cos \phi, V_r \cos \theta - V_\theta \sin \theta]$. As $\vec{e}_r = \frac{\vec{r}}{|\vec{r}|} = [\sin \theta \cos \phi, \sin \theta \sin \phi, \cos \theta]$ and $\vec{r}_\odot = [r_\odot, 0, 0]$ the l.o.s versor is $\vec{e}_\rho \equiv \frac{\vec{r} - \vec{r}_\odot}{|\vec{r} - \vec{r}_\odot|} = \frac{[r \sin \theta \cos \phi - r_\odot, r \sin \theta \sin \phi, r \cos \theta]}{\sqrt{r^2 + r_\odot^2 - 2r r_\odot \sin \theta \cos \phi}}$.

We take the mean values $\langle v_r^2 \rangle \equiv \langle (\vec{e}_r \circ \vec{v})^2 \rangle$ and $\langle \tilde{v}_r^2 \rangle \equiv \langle (\vec{e}_\rho \circ \vec{v})^2 \rangle$ over thin spherical shells and consider them as functions of the Galacto-centric distance r . For a spheri-

cally symmetric system we define $\langle \tilde{v}_r^2(r) \rangle$ as

$$\langle \tilde{v}_r^2(r) \rangle = \frac{1}{4\pi \nu(r)} \int_0^\pi d\theta \sin \theta \int_0^{2\pi} d\phi \langle (\vec{e}_\rho(r, \theta, \phi) \circ \vec{v})^2 \rangle_{\text{int}}.$$

Here, $\langle \cdot \rangle_{\text{int}}$ is the averaging over the velocities weighted by a spherically symmetric *PDF* $f(r, \vec{v}(r))$, normalized so as $\nu(r) \langle (\cdot) \rangle_{\text{int}} \equiv \int (\cdot) f(r, \vec{v}(r)) d^3 \vec{v}$, with ν denoting the number density. The scalar product squared $(\vec{e}_\rho(r, \theta, \phi) \circ \vec{v})^2$ is a homogenous form of second degree in the velocities V_r, V_θ, V_ϕ with coefficients being functions of r, θ, ϕ . By a direct inspection one can notice that the integration over θ, ϕ of the coefficients standing at $V_r V_\theta, V_\theta V_\phi, V_\phi V_r$, gives zero (the velocity products are independent of θ, ϕ). Thus, upon integration over the velocities, we can focus only on the terms involving dispersions $\langle V_r^2 \rangle(r), \langle V_\theta^2 \rangle(r), \langle V_\phi^2 \rangle(r)$. Furthermore, it also follows from the spherical symmetry that $\langle V_\phi^2 \rangle(r) = \langle V_\theta^2 \rangle(r)$ and, trivially, that the ratios $\langle V_\theta^2 \rangle / \langle V_r^2 \rangle, \langle V_\phi^2 \rangle / \langle V_r^2 \rangle$ define the same function of r . In accordance with the common convention in the theory of spherical Jeans equations, we express this function in terms of the flattening of the dispersion ellipsoid, $\beta(r)$. Then, by making the substitution $\langle V_\theta^2 \rangle(r) = (1 - \beta(r)) \langle V_r^2 \rangle(r)$ and $\langle V_\phi^2 \rangle(r) = (1 - \beta(r)) \langle V_r^2 \rangle(r)$, we obtain that

$$\langle \tilde{v}_r^2 \rangle(r) = \langle v_r^2 \rangle(r) \left(1 - \frac{\beta(r)}{1 + r^2/r_\odot^2} \cdot \mathcal{I}(\alpha(r)) \right),$$

where $\alpha(r) \equiv \frac{2r r_\odot}{r^2 + r_\odot^2} < 1$ for $r \neq r_\odot$ and

$$\mathcal{I}(\alpha) = \frac{1}{4\pi} \int_0^\pi d\theta \int_0^{2\pi} d\phi \frac{\sin \theta (\cos^2 \theta \cos^2 \phi + \sin^2 \phi)}{1 - \alpha \sin \theta \cos \phi}.$$

We recall that all integrals that are zero by symmetries have been already omitted in the expression for $\mathcal{I}(\alpha)$. On account that the requirements for the integration of a functional series term by term and its limit are met for $0 \leq \alpha < 1$, the integral $\mathcal{I}(\alpha)$ can be calculated by a Taylor series expansion in α (note that owing to the vanishing of the integrals $\int_0^{2\pi} \cos^m \phi d\phi$ with odd m , only even powers of α are present in the series). On reducing the summands with the help of the Pythagorean trigonometric identity, the remaining nonzero coefficients in the power series in α arrange to products of elementary definite integrals $\mathcal{I}(\alpha) = \frac{1}{4\pi} \sum_{n=0}^{+\infty} \alpha^{2n} (S_n C_n - S_{n+1} C_{n+1})$, where $S_n = \int_0^\pi \sin^{2n+1} \theta d\theta = 2 \frac{(2n)!!}{(2n+1)!!}$; $C_n = \int_0^{2\pi} \cos^{2n} \phi d\phi = 2\pi \frac{(2n-1)!!}{(2n)!!}$. Now, $C_n S_n = \frac{4\pi}{2n+1}$ and $C_{n+1} S_{n+1} = \frac{4\pi}{2n+3}$. Hence, $\mathcal{I}(\alpha) = \frac{1}{2\alpha} \sum_{n=0}^{\infty} \frac{2\alpha^{2n+1}}{2n+1} - \frac{1}{2\alpha^3} \left(-2\alpha + \sum_{n=0}^{\infty} \frac{2\alpha^{2n+1}}{2n+1} \right)$, where we have subtracted the excess term 2α in the second series after renaming $n \rightarrow n+1$. Both of the infinite series are Taylor series expansions of $\ln \frac{1+\alpha}{1-\alpha}$, therefore

$$\mathcal{I}(\alpha) = \frac{1}{\alpha^2} - \frac{1-\alpha^2}{2\alpha^3} \ln \left(\frac{1+\alpha}{1-\alpha} \right), \quad 0 \leq \alpha < 1.$$

Next, using the earlier expression for $\langle \tilde{v}_r^2 \rangle$ and substituting the definition of $\alpha(r)$ in place of α , we finally obtain Eq. 2-5.

B. Derivation of the equations of motion from a nonstandard Hamiltonian

In this section we use cylindrical coordinates (ρ, φ, ζ) . By axial symmetry of the potential $\Psi(\rho, \zeta)$ the J_φ component of the angular momentum is conserved. Thus, we may use φ as the independent parameter for trajectories with $J_\varphi \neq 0$. Then the Lagrangian for a test body of mass m attains the form $L = \frac{m}{2} \frac{\rho'(\varphi)^2 + \rho^2 + \zeta'(\varphi)^2}{t'(\varphi)} - m \Psi(\rho, \zeta) t'(\varphi)$. The dynamical variables, which we now regard as functions of φ , are ρ , ζ and the time variable t . The Hamiltonian is found, as usual, by means of the Legendre transformation $L \rightarrow G \equiv \rho'(\varphi) \frac{\partial L}{\partial \rho'(\varphi)} + \zeta'(\varphi) \frac{\partial L}{\partial \zeta'(\varphi)} + t'(\varphi) \frac{\partial L}{\partial t'(\varphi)} - L = -\frac{m \rho^2}{t'(\varphi)}$, where the velocities must be expressed in terms of positions and momenta. Solving the canonical definitions of momenta $p_\rho = \frac{\partial L}{\partial \rho'(\varphi)} = m \frac{\rho'(\varphi)}{t'(\varphi)}$, $p_\zeta = \frac{\partial L}{\partial \zeta'(\varphi)} = m \frac{\zeta'(\varphi)}{t'(\varphi)}$, and $p_t = \frac{\partial L}{\partial t'(\varphi)} = -m \frac{\rho'(\varphi)^2 + \rho^2 + \zeta'(\varphi)^2}{2t'(\varphi)^2} - m \Psi(\rho, \zeta)$ for velocities, we find that the Hamiltonian H reads

$$H = \pm \rho \sqrt{-\left(p_\rho^2 + 2m p_t + p_\zeta^2 + 2m^2 \Psi(\rho, \zeta)\right)}.$$

For solutions, this Hamiltonian equals minus the third component of the angular momentum (!). Since H is not an explicit function of φ , H is constant for solutions. Let denote this constant by $-J_\varphi$. Because there are two solutions for H with the opposite sign and H is constant for solutions, it is more convenient to rewrite Hamiltonian equations into the reduced form $q'(\varphi) = -\frac{1}{2J_\varphi} \{q, H^2\}$, $p'(\varphi) = -\frac{1}{2J_\varphi} \{p, H^2\}$, where $\{, \}$ is the Poisson bracket on the phase space $(\rho, p_\rho, \zeta, p_\zeta, t, p_t)$. In explicit form these equations read: $\rho'(\varphi) = \frac{p_\rho^2}{J_\varphi} p_\rho$, $\zeta'(\varphi) = \frac{p_\zeta^2}{J_\varphi} p_\zeta$, $t'(\varphi) = \frac{p_t^2}{J_\varphi} m$, $p_\rho'(\varphi) = \frac{J_\varphi}{\rho} - \frac{m^2 \rho^2}{J_\varphi} \partial_\rho \Psi$, $p_\zeta'(\varphi) = -\frac{m^2 \rho^2}{J_\varphi} \partial_\zeta \Psi$, $p_t'(\varphi) = 0$. The last equation states that p_t is conserved. We denote this constant value by $-E$. Then, using the expression for H^2 or the definition of p_t along with the Hamiltonian equations, it follows that $E = \frac{1}{2m} \left(p_\rho^2 + p_\zeta^2 + J_\varphi^2 / \rho^2\right) + m \Psi(\rho, \zeta)$. The solution for function $t(\varphi)$ is not important for our purposes – the time averages along a trajectory may be expressed as averages over the angle φ , namely $\frac{1}{T} \int_0^T F(t) dt = \frac{\int F \rho^2 d\varphi}{\int \rho^2 d\varphi}$. Therefore, given constants J_φ and E , and having specified the initial conditions consistently with E and J_φ , only four independent equations are left to be solved. On expressing p_ρ and p_ζ by the physical velocities $v_\rho \equiv \frac{\rho'(\varphi)}{t'(\varphi)}$ and $v_\zeta \equiv \frac{\zeta'(\varphi)}{t'(\varphi)}$, the remaining first order equations for four functions $v_\rho(\varphi)$, $v_\zeta(\varphi)$, $\rho(\varphi)$ and $\zeta(\varphi)$ reduce to:

$$\begin{aligned} \rho'(\varphi) &= \frac{\rho^2}{J_\varphi/m} v_\rho, & v_\rho'(\varphi) &= \frac{J_\varphi/m}{\rho} - \frac{\rho^2}{J_\varphi/m} \partial_\rho \Psi(\rho, \zeta), \\ \zeta'(\varphi) &= \frac{\rho^2}{J_\varphi/m} v_\zeta, & v_\zeta'(\varphi) &= -\frac{\rho^2}{J_\varphi/m} \partial_\zeta \Psi(\rho, \zeta), \end{aligned}$$

and the energy integral attains the form

$$E/m = \frac{v_\rho^2}{2} + \frac{v_\zeta^2}{2} + \frac{(J_\varphi/m)^2}{2\rho^2} + \Psi(\rho, \zeta).$$

REFERENCES

- Bahcall, J. N. & Tremaine, S. 1981, ApJ, 244, 805
- Battaglia, G., Helmi, A., Morrison, H., et al. 2005, MNRAS, 364, 433
- Beers, T. C., Preston, G. W., & Shectman, S. A. 1992, AJ, 103, 1987
- Belokurov, V., Walker, M. G., Evans, N. W., et al. 2008, ApJ, 686, L83
- Belokurov, V., Walker, M. G., Evans, N. W., et al. 2009, MNRAS, 397, 1748
- Bratek, L., Sikora, S., Jalocho, J., & Kutschera, M. 2014, A&A, 562, A134
- Clewley, L., Warren, S. J., Hewett, P. C., Norris, J. E., & Evans, N. W. 2004, MNRAS, 352, 285
- Deason, A. J., Belokurov, V., Evans, N. W., & An, J. 2012a, MNRAS, 424, L44
- Deason, A. J., Belokurov, V., Evans, N. W., et al. 2012b, MNRAS, 425, 2840
- Dohm-Palmer, R. C., Helmi, A., Morrison, H., et al. 2001, ApJ, 555, L37
- Geha, M., Willman, B., Simon, J. D., et al. 2009, ApJ, 692, 1464
- Gradshteyn, I., Ryzhik, I., Jeffrey, A., & Zwillinger, D. 2007, Table of integrals, series and products, Academic Press
- Gupta, A., Mathur, S., Krongold, Y., Nicastro, F., & Galeazzi, M. 2012, ApJ, 756, L8
- Harris, W. E. 1996, AJ, 112, 1487
- Jalocho, J., Sikora, S., Bratek, L., & Kutschera, M. 2014, A&A, 566, A87
- Jeans, J. H. 1915, MNRAS, 76, 70
- Kaffe, P. R., Sharma, S., Lewis, G. F., & Bland-Hawthorn, J. 2014, ApJ, 794, 59
- Klypin, A., Zhao, H., & Somerville, R. S. 2002, ApJ, 573, 597
- Koch, A., Wilkinson, M. I., Kleyna, J. T., et al. 2009, ApJ, 690, 453
- Kochanek, C. S. 1996, ApJ, 457, 228
- Little, B. & Tremaine, S. 1987, ApJ, 320, 493
- Magorrian, J. 2014, MNRAS, 437, 2230
- Martin, N. F., Ibata, R. A., Chapman, S. C., Irwin, M., & Lewis, G. F. 2007, MNRAS, 380, 281
- Mateo, M. L. 1998, ARA&A, 36, 435
- Merrifield, M. R. 1992, AJ, 103, 1552

- Miller, M. J. & Bregman, J. N. 2013, *ApJ*, 770, 118
- Morrison, H. L., Mateo, M., Olszewski, E. W., et al. 2000, *AJ*, 119, 2254
- Newberg, H. J., Willett, B. A., Yanny, B., & Xu, Y. 2010, *ApJ*, 711, 32
- Sakamoto, T., Chiba, M., & Beers, T. C. 2003, *A&A*, 397, 899
- Sesar, B., Grillmair, C. J., Cohen, J. G., et al. 2013, *ApJ*, 776, 26
- Sikora, S., Bratek, L., Jałocha, J., & Kutschera, M. 2012, *A&A*, 546, A126
- Simon, J. D. & Geha, M. 2007, *ApJ*, 670, 313
- Starkenburger, E., Helmi, A., Morrison, H. L., et al. 2009, *ApJ*, 698, 567
- Watkins, L. L., Evans, N. W., & An, J. H. 2010, *MNRAS*, 406, 264
- Wilhelm, R., Beers, T. C., Sommer-Larsen, J., et al. 1999, *AJ*, 117, 2329
- Wilkinson, M. I. & Evans, N. W. 1999, *MNRAS*, 310, 645
- Xue, X. X., Rix, H. W., Zhao, G., et al. 2008, *ApJ*, 684, 1143